Improving Forecasts of Persistent Contrails through Ice Deposition Adjustments

Zane Dedekind[1], Alexei Korolev[1], and Jason A. Milbrandt[1]

[1]Meteorological Research Division, Environment and Climate Change Canada, Toronto, Ontario, Canada

Correspondence: Zane Dedekind (zane.dedekind@ec.gc.ca)

Abstract. Aviation-induced clouds, especially persistent contrails, contribute significantly to anthropogenic climate forcing, often surpassing the short-term impact of aviation CO_2 emissions. These clouds form in ice-supersaturated regions, where they trap longwave radiation and warm the climate. On 25 November 2023, widespread ice-supersaturated layers over eastern Canada and the USA led to extensive contrail formation, confirmed by GOES-16 satellite imagery and ground-based pho-
5 tography. Atmospheric conditions were characterized using ceilometer data from Toronto Pearson Airport and radiosonde soundings.

High-resolution simulations were conducted using the Global Environmental Multiscale (GEM) model with the Predicted Particle Properties (P3) microphysics scheme. The Contrail Avoidance Tool (CoAT), incorporating Schmidt-Appleman Criteria and a wake vortex model, simulated persistent contrail formation and properties. Sensitivity tests adjusting ice depositional
10 growth rates evaluated their impact on ice supersaturation. Results indicate that the control (CNTL) simulation underestimated relative humidity over ice (RH_i), a common limitation where moisture is depleted too rapidly. Reduced depositional growth rates improved RH_i forecasts and contrail-forming regions. However, GEM-CoAT underestimated contrail depth and ice number concentration in very shallow high-RH_i layers. CoAT simulations also revealed that SAC alone is insufficient, as wake vortex dynamics can induce adiabatic warming, leading to ice particle sublimation.
15 Further analysis examined contrail formation for two aircraft types (A321 and B747). The B747 generated deeper wake vortices, enhancing adiabatic heating and reducing contrail ice number concentrations by 27% in sensitivity simulations and 78% in the CNTL simulations. Adjusting depositional growth rates allowed GEM-CoAT to accurately simulate contrail formation and persistence.

20 # 1 Introduction

Contrails, or condensation trails, are linear ice clouds that form in the wake of aircraft flying at high altitudes where the ambient atmosphere is sufficiently cold, typically colder than $-40\,°C$, and humid. These artificial clouds originate from the mixing of hot, moist exhaust gases with the surrounding air, leading to rapid condensation and freezing of water vapor onto emitted

particles, such as soot and other aerosols (Schumann, 1996; Kärcher, 2018). While some contrails dissipate quickly, others

25 persist and spread into contrail cirrus if the environmental air is ice-supersaturated, which can contribute to cloud cover and significantly alter the radiative balance of the Earth's atmosphere (Kärcher, 2018; Lee et al., 2023).

The aviation industry is a significant contributor to anthropogenic climate change, accounting for approximately 3.5 % of total effective radiative forcing (ERF) as of 2018 (Kärcher, 2018; Lee et al., 2021). Notably, about two-thirds (66 %) of this warming impact is attributed to non-CO_2 effects, primarily from contrail cirrus and nitrogen oxide (NO_x) emissions. The

30 radiative forcing from contrail cirrus alone is estimated to be $57.4 \, \text{mW m}^{-2}$, making it the single largest contributor to aviation-induced climate effects, surpassing the impact of cumulative CO_2 emissions from aviation, which is $34.3 \, \text{mW m}^{-2}$ (Lee et al., 2021).

Contrail cirrus exerts a complex influence on Earth's energy balance. While they reflect some incoming solar radiation, their primary effect is trapping outgoing longwave radiation, leading to a net warming impact. The strength of this effect depends

35 on atmospheric conditions, contrail properties, and flight patterns. Studies indicate that contrail-induced cloudiness covers up to 10 % of the sky area in high-traffic regions such as Europe and North America (Burkhardt and Kärcher, 2011).

Given the projected growth in global aviation, expected to double its CO_2 emissions by 2050 without mitigation strategies (Lee et al., 2009), understanding and addressing contrail-induced climate effects is a critical research priority. Several mitigation strategies have been explored, including optimizing flight altitudes and routes, reducing soot emissions by transitioning to

40 low-aromatic or biofuel blends, using hydrogen fuels, and employing alternative aircraft propulsion technologies (Burkhardt et al., 2018; Teoh et al., 2020, 2022; Lottermoser and Unterstraßer, 2025). Studies suggest that targeted rerouting of just 2 % of flights could reduce contrail radiative forcing by up to 59 % with negligible fuel penalties over Japanese airspace while rerouting 12 % of flight reduce the radiative forcing by 80 % over the North Atlantic (Teoh et al., 2020, 2022).

45 Simulating the evolution of contrail ice number concentration (CINC) is crucial for accurately predicting contrail persistence and lifetime. Ice crystal number concentration directly influences contrail optical depth, growth rates, and sedimentation, which in turn determine their overall climate impact. Higher CINCs lead to greater optical thickness and longer persistence, whereas lower CINCs promote faster ice particle sedimentation and sublimation, reducing contrail lifespan. Several parameterizations have been developed to better represent contrail microphysics and ice crystal evolution. Schumann (2012) introduced

50 the Contrail Cirrus Prediction Tool (CoCiP), a fast process-based model designed to estimate contrail properties based on meteorological conditions and aircraft emissions. Lewellen and Lewellen (2001); Lewellen et al. (2014) applied large-eddy simulations to investigate wake vortex dynamics and their impact on contrail ice crystal formation, showing how turbulence influences contrail spreading and persistence. Unterstrasser (2016) developed a parameterization that enhances the representation of contrail-to-cirrus transitions, improving the understanding of how environmental conditions, including ice supersaturation,

55 affect contrail growth and dissipation.

The persistence and variability of ice supersaturation in ice clouds are strongly influenced by the deposition coefficient (α_D), which describes the efficiency of water vapor molecules attaching to ice crystal surfaces. Laboratory studies, including wind

tunnel experiments, cloud chambers, and cold-stage scanning electron microscopy imaging, have shown that α_D is not constant
60   but varies with temperature, supersaturation, and ice crystal habit. Measurements by Fukuta and Takahashi (1999), Lamb
et al. (2023), and Harrington and Pokrifka (2024) reveal that α_D often falls well below unity under cold, upper-tropospheric
conditions typical of cirrus, indicating kinetic limitations to depositional growth. These studies also identify supersaturation
thresholds associated with morphological transitions such as hollowing, providing physical constraints on when and how
efficiently crystals grow.

65   From a modeling perspective, simplified treatments that assume $\alpha_D = 1$ or apply saturation adjustment fail to capture the
observed frequency and magnitude of ice-supersaturated regions. Gierens et al. (2003, 2020) and (Sperber and Gierens, 2023)
showed that such assumptions result in systematic underprediction of supersaturation and contrail persistence in numerical
weather and climate models. To address this, Kärcher et al. (2023) incorporated supersaturation-dependent deposition coef-
ficients, based on laboratory constraints from Lamb et al. (2023), into stochastic parcel models coupled with gravity wave-
70   induced temperature fluctuations. Their simulations reproduced both the mean and variability of in situ supersaturation mea-
surements, highlighting the role of depositional kinetics in ice cloud microphysics. Together, laboratory and modeling work
shows the need for physically-based representations of α_D to accurately simulate ice cloud evolution.

This study investigates how variations in the depositional growth of ice, calculated by adjusting α_D, affect the extent and
75   persistence of ice-supersaturated regions and the properties of contrails within a high-resolution numerical weather prediction
framework. We explore the following questions:

- How does the adjustment of the ice deposition rate, through changes in the deposition coefficient, influence the persis-
tence and intensity of ice-supersaturated regions?

- In what ways does the deposition rate impact contrail formation processes and the resulting CINC within young contrails?

80   - To what extent do wake vortex dynamics, particularly adiabatic heating during plume descent, limit contrail formation
despite favorable Schmidt–Appleman Criteria (SAC) conditions?

The remainder of this paper is organized as follows: Section 2 describes the methods, including an overview of the synoptic
environment, observational datasets, and the modeling tools used to simulate contrail formation. Section 3 presents the results
of sensitivity experiments examining how variations in the depositional growth rate affect the RH_i, contrail ice number concen-
85   trations, and contrail persistence. Section 4 discusses the implications of these findings. The paper concludes with a summary
of key findings and recommendations for improving contrail representation in weather and climate models. Appendix A pro-
vides the physical basis and equations governing the depositional growth of ice crystals and how the deposition coefficient α_D
influences ice particle mass growth under supersaturated conditions.

2 Methods

2.1 Synoptic conditions and observational data

On 25 Nov 2023, a large ice-supersaturated region formed, leading to extensive cirrus cloud formation over the southeastern and northeastern parts of Canada and the USA, respectively. The upper-level atmospheric conditions included a deep trough in the jet stream which allowed cold Arctic air to plunge southward into the Great Lakes region. This created significant temperature contrasts and instability in the upper troposphere. Evidence from radiosonde soundings, satellite observations, and surface-based photography confirmed the presence of ice-supersaturated layers aloft, within which cirrus clouds and persistent contrails formed (Fig. 1b-d).

2.1.1 Radiosonde data

Upper-air radiosonde data were obtained from the University of Wyoming dataset (University of Wyoming, 2024). The radiosonde data encompassed the balloon's precise trajectory, detailing latitude, longitude, altitude, and time. This information is crucial, as radiosondes can drift significantly from their launch sites during ascent. Balloons may drift approximately 5 km in the mid-troposphere, around 20 km in the upper troposphere (Seidel et al., 2011). Radiosonde data was collected to determine the drift distance between the launch location and the 300 hPa pressure level (approximately jet cruising altitude) for various stations at 1200 UTC on 25 November 2023 (Table 1).

Table 1. Radiosonde Drift Distances at 300 hPa at 1200 UTC on 25 Nov 2023

Station Name	Location	Station Identifier	Drift Distance (km)
Albany	NY, USA	ALB	31.23
Gaylord	MI, USA	APX	25.22
Buffalo	NY, USA	BUF	23.23
White Lake	MI, USA	DTX	19.96
Green Bay	WI, USA	GRB	23.44
International Falls	MN, USA	INL	34.12
Maniwaki	QC, Canada	WMW	42.42
Pickle Lake	ON, Canada	WPL	41.82

Assuming a balloon ascent rate of $5 \, \text{m s}^{-1}$, the time to reach the 300 hPa pressure level is approximately 30.5 min if the balloon drift is ignored. However, considering potential variations in ascent rates and balloon drift, the actual time can range between 40 min and 110 min. For modeling purposes, we assume an ascent time of approximately 50 min to align the model data with the balloon's arrival at the 300 hPa level.

2.1.2 Satellite data

110 The Advanced Baseline Imager (ABI) aboard the GOES-R series satellites is a passive imaging radiometer featuring 16 spectral bands, including 10 in the infrared spectrum. The spatial resolution for these infrared bands is 2 km (Kalluri et al., 2018). In its operational modes, the ABI provides full-disk imagery every 10 min, images of the contiguous United States (CONUS) every 5 min, and two mesoscale images every 60 s (or one every 30 s). Among its capabilities, the ABI utilizes a "Dust" RGB (Red-Green-Blue) composite to detect and monitor airborne dust. This product is also especially useful to detect contrails. This

115 composite combines data from infrared channels 8.4 μm (Band 11), 10.3 μm (Band 13) and 12.3 μm (Band 15). The GOES-16 data was downloaded from University of Utah (2020) and the "Dust" RBG was generated using the software package from Blaylock (2023).

2.1.3 Aircraft flight data

- **Data Source:** Flight data was obtained from Flightradar24 (Flightradar24, 2024).

120 - **Selected Flights:** A subset of flights was identified as potential contributors to contrail formation (Fig. 1 and Table 2). These flights cruised at altitudes ranging from 8,800 m to 10,700 m (29,000 ft to 35,000 ft).

- **Recorded Data Points:** Flight data was recorded at 30 s intervals, during which aircraft traveled approximately 6 to 7 km at cruising speed between recordings. The data was then interpolated onto a 1 km × 1 km grid, aligning with the model grid resolution, ensuring one recording per grid point.

Table 2. Aircraft Wingspan and Cruising Altitude Data

Aircraft Identifier	Aircraft Type	Wingspan (m)	Cruising Altitude (ft)	~Time of Toronto Flyover (UTC)
TK6061	**B747**	**64.4**	**31,000**	**1345**
CV6686	**B747**	**64.4**	**34,000**	**1315**
AS459	B747	64.4	34,000	1330
DL384	**A321**	**35.8**	**30,000–34,000**	**1245**
AA2455	A321	35.8	34,000	1330
UA364	A319	35.8	34,000	1415
UA311	B757	38.0	34,000	1345

125 ### 2.1.4 Ceilometer at CYYZ

The Ceilometer, CHM 15k Cloud Height Meter, is an advanced light detection and ranging (LIDAR-based) remote sensing instrument deployed at Toronto Pearson International Airport (CYYZ) to measure cloud height, penetration depth, and vertical visibility. Operating at a 15 s temporal resolution, it employs the lidar technique to emit short laser pulses into the atmo-
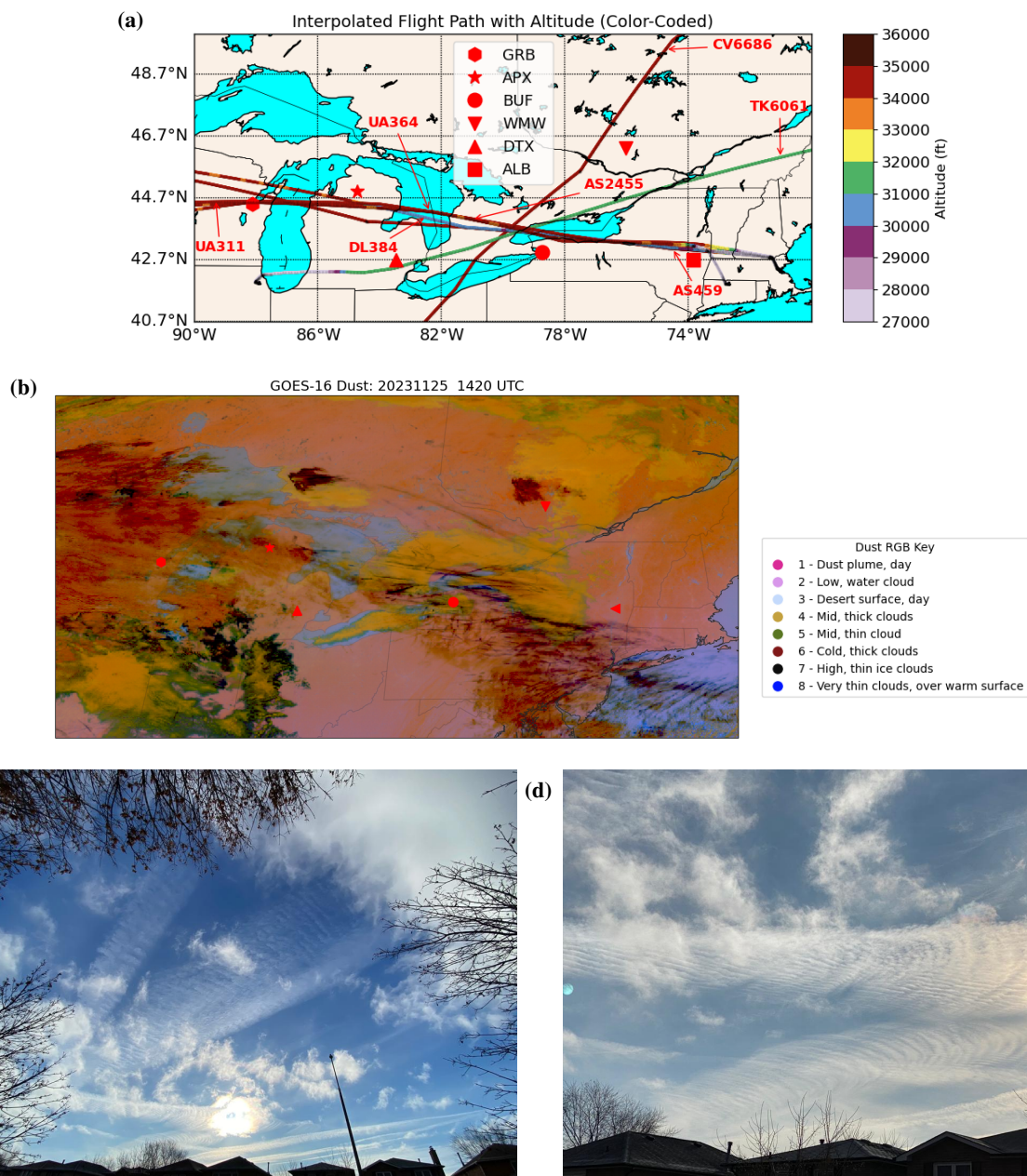
Figure 1. (a) Interpolated flight paths and sounding stations **(b)** GOES-16 Dust RGB and sounding stations at 1430 UTC **(c)** and **(d)** photos taken from Toronto, Canada at 1420 UTC by Alexei Korolev.

sphere. These pulses scatter upon interaction with aerosols and cloud particles, with the backscattered signal being analyzed to
130   determine cloud structure and visibility conditions.

The CHM 15k is capable of measuring up to 15 km in altitude with a range resolution of 5–15 m, depending on the measurement mode. Its full waveform analysis allows for the identification of multiple cloud layers (up to 9), 3 layers in its current configuration, and provides high-resolution backscatter profiles. It utilizes photon counting technology, enhancing detection sensitivity and minimizing background noise. The system records parameters such as cloud base height, penetration depth, maximum detectable range, vertical visual range, and sky condition, making it crucial for aviation meteorology and atmospheric research.

2.2 Model

2.2.1 Atmospheric model and initialization

The Global Environmental Multiscale (GEM) model is a versatile atmospheric modeling system widely used for high-resolution simulations of atmospheric processes (Côté et al., 1998; Girard et al., 2014). The integration of the Predicted Particle Properties (P3) microphysics scheme into GEM represents a significant advancement in the modeling of ice-phase hydrometeors and mixed-phase cloud dynamics. This methodology outlines the configuration and application of the GEM-P3 setup as described in several studies (Morrison and Milbrandt, 2015; Milbrandt and Morrison, 2016; Milbrandt et al., 2021; Qu et al., 2022; Cholette et al., 2024; Korolev et al., 2024).

GEM has a non-hydrostatic, fully compressible dynamical core using semi-Lagrangian advection and a terrain-following hybrid vertical coordinate system (Côté et al., 1998; Girard et al., 2014). This configuration is suitable for a wide range of resolutions, from mesoscale to cloud-resolving scales. Our simulations use a horizontal grid spacings of $1 \, km \times 1 \, km$ over a 1600×1000 domain centered at $45.2 \, °N$ and $-79.9°E$ (eastern Canada). Typically, 60 vertical levels are used in operational systems using GEM, but here 121 vertical levels are used to enhance the vertical resolution in the upper tropical troposphere with grid spacings of $\sim 230 \, m$ at $300 \, hPa$ to capture ice supersaturated regions better. GEM uses lateral and surface boundary conditions obtained from the operational 2.5-km High Resolution Deterministic Prediction System (HRDPS; Milbrandt et al., 2016), which is updated hourly. A $30 \, s$ model timestep is used, with the model initialized at $0600 \, UTC$ and running for a duration of $13 \, h$.

2.2.2 Cloud microphysics scheme

The P3 microphysics scheme is unique in that the ice phase uses the property-based approach, in contrast with the traditional approach of predefined ice-phase categories, whereby all ice-phase or mixed-phase particles are represented by one or more generic or "free" categories whose bulk physical properties evolve freely and continuously. This enables each ice category to represent a wide range of dominant types of ice. With the use of multiple free ice-phase categories, multiple modes – i.e. populations of ice with different bulk properties – can exist in the same point in time and space. A complete description of the original P3 scheme can be found in Morrison and Milbrandt (2015) and Milbrandt et al. (2016); descriptions of subsequent

7

major developments can be found in Milbrandt et al. (2021), Cholette et al. (2024), and Morrison et al. (2025). In this study, the two-moment ice configuration, with prognostic liquid fraction off, and with 3 ice categories is used.

165   Hydrometeor size distributions are represented by complete 3-parameter gamma functions, with shape and slope parameters evolving dynamically based on the prognostic variables. The configuration uses the two-moment treatment of ice particles instead of the triple-moment treatment which is more relevant for deep convective systems to better resolve size sorting and improve simulations of hail and heavily rimed particles. Additionally, at the time of preparing this study, the "full" 3-moment version of P3 Morrison et al. (2025) was not yet available. In this version, the spectral dispersion changes due to deposition/-

170   sublimation which could be a topic of future work for contrails.

To examine the impact of the deposition coefficient (α_D, from equation A2) on the mass growth of ice crystals (equation A1) and its subsequent effect on contrail persistence, we conducted sensitivity simulations. These simulations introduce reduction factors (rf) to adjust the depositional growth of ice particles heuristically.

175
$$\frac{\left(\frac{dm}{dt}\right)_{\alpha_D}}{\left(\frac{dm}{dt}\right)_{\alpha_D=1}} = rf, \quad \text{where} \quad rf \in \{0.6, 0.8, 0.9\} \tag{1}$$

The reduction factor rf is determined by varying the ice particle size and computing the corresponding α_D. These size-dependent α_D values are then used to calculate the depositional growth rate, which is subsequently compared to the reference case where $\alpha_D = 1$ in the depositional growth rate equation. Further information on this approach can be found in Appendix A.

180   ### 2.2.3   Contrail model: CoAT

The formation of contrails, governed by the Schmidt–Appleman Criterion (SAC), requires specific thermodynamic conditions that depend on both atmospheric and aircraft parameters. A critical parameter in this framework is the slope of the mixing line, G, which characterizes the relationship between the exhaust plume and the ambient atmosphere. According to Schumann (2012), G is expressed as:

185
$$G = \frac{c_p \cdot p \cdot EI_{H_2O}}{\left(\frac{M_{H_2O}}{M_{\text{air}}}\right) \cdot Q \cdot (1-\eta)}, \tag{2}$$

where c_p is the specific heat capacity of air at constant pressure (1004 J kg^{-1} K^{-1}), p is the ambient pressure (Pa), EI_{H_2O} is the water emission index (kg of H_2O per kg of fuel burned), M_{H_2O}/M_{air} is the molar mass ratio of water to air (approximately 0.622), Q is the specific combustion heat of the fuel (43.2 MJ kg^{-1} for kerosene), and η is the propulsion efficiency (0.29).

For contrails to form, the ambient temperature T must be below the maximum threshold temperature, defined as the tem-

190   perature at which the mixing line intersects the liquid water saturation curve (Schumann, 2012). Additionally, the relative humidity over water must exceed the critical threshold to ensures that the water vapor in the exhaust can condense. Under

8

these conditions, water vapor condenses and freezes on aerosols, forming ice particles. These ice particles grow by water vapor deposition, and if ice supersaturation persists, the contrails can evolve into long-lived clouds.

The wake vortex phase of contrail evolution involves distinct processes in the primary and secondary wakes, critical for understanding contrail dynamics and their transition into cirrus clouds. The primary wake, associated with the counter-rotating vortex pair generated by the aircraft's lift, experiences strong downward motion, leading to adiabatic heating and partial sublimation of ice particles. These dynamics, which trap a significant portion of the exhaust within the vortex pair, are strongly influenced by environmental factors such as temperature and relative humidity (Sussmann and Gierens, 1999; Unterstrasser, 2016). In contrast, the secondary wake forms a "curtain" of detrained exhaust between the original emission altitude and the descending vortex. Ice particles in the secondary wake grow through deposition in an ice-supersaturated environment and retain the majority of the contrail ice mass by the end of the vortex phase. This secondary wake, less affected by adiabatic heating, plays a crucial role in the persistence and spreading of contrails (Unterstrasser, 2014; Lewellen et al., 2014; Unterstrasser, 2016).

When the conditions for T and RH_i from the SAC are satisfied, GEM uses the wake vortex model from Unterstrasser (2016), which focuses on the interaction between ice microphysics and wake vortex dynamics. The Unterstrasser (2016) parameterization provides a framework for quantifying key characteristics of young contrails during their early development phases. It calculates the maximum vertical displacement of wake vortices and the vertical extent of the contrail, which corresponds to the maximum vortex displacement if ice particles can survive the warming effects associated with the adiabatic descent of the vortices. Additionally, it estimates the survival fraction of contrail ice particles, accounting for their loss due to changes in relative humidity resulting from adiabatic warming and incorporating the influence of ice supersaturation, temperature, and the Kelvin effect on crystal growth (Jensen et al., 2024). The wake vortex model uses the aircraft information from Table 2 and the atmospheric conditions (e.g. temperature, pressure, humidity and the static stability of air) from GEM to determine ice particle survival, the contrail ice number concentration and the vertical contrail extent of young contrails during the first 5 min. The wake vortex model enables parameterizations to incorporate additional aircraft characteristics, such as weight, speed, and fuel flow rate. However, for our purposes, we utilized only the parameterization based on wingspan for further calculations. To estimate the contrail ice mass concentration, the sublimated ice particles from the primary vortex are converted into water vapor and incorporated into the plume's water vapor budget. The surviving ice particles grow through deposition, assuming spherical geometry for the ice particles (Pruppacher and Klett, 2010). The resulting contrail ice number and mass concentrations derived from the wake vortex model are subsequently advected by GEM. If the contrail's vertical extent exceeds that of the model grid, the contrail's ice content is distributed into the model grid box below the flight level (Appendix A2).

3 Results

Here, we present two distinct simulation approaches, along with the sensitivity simulations, for analyzing contrail formation. First, we conducted simulations assuming the characteristics of an A321 aircraft and a B747 aircraft uniformly across the entire

225 domain. This approach allowed us to generate metrics such as contrail depth, contrail ice number concentration (CINC), and ice particle survival (IPS) at each timestep, as if an A321 or B747 were present throughout the domain. This methodology provides insights into potential contrail formation areas within the domain. The outcomes of these simulations are discussed in Sections 3.1.3 and 3.2.1. Second, we performed simulations where the model utilized actual flight data to extract specific aircraft locations and timings. Contrail characteristics were then simulated exclusively along the recorded flight paths, based
230 on the aircraft properties detailed in Table 2. These findings are elaborated in Section 3.2.2.

3.1 Depositional growth sensitivity simulations

3.1.1 RHi distribution: Sounding vs GEM

The approach examines the relationship between ice particle growth rates and RH_i by analyzing soundings and comparing them to simulations from the GEM model. The simulations are designed to illustrate how variations in ice particle growth rates
235 influence RH_i. By contrasting the sounding observations with GEM under different growth rate scenarios, we aim to elucidate the impact of ice particle depositional growth on atmospheric humidity profiles. To account for uncertainty in balloon drift, a $30\,km \times 30\,km$ area surrounding balloon location while ascending was used to compile the vertical profile for each station in GEM's output, which is then compared to the soundings.

Figure 2 presents the RH_i distribution for sounding observations compared to GEM at $1200\,UTC$ on 25 Nov 2023, consid-
240 ering pressure levels between $100\,hPa$ and $600\,hPa$ and temperatures colder than $-38\,°C$. The simulations capture the general distribution well below an RH_i of $100\,\%$ when compared to the all-soundings distribution. However, as RH_i approaches $100\,\%$, GEM underestimates the probability of higher RH_i values, particularly in the supersaturation range, where it fails to capture the frequency and intensity of ice supersaturation events. The combined sounding RH_i distribution peaks at $100\,\%$ and then gradually decreases, reaching a maximum RH_i of $145\,\%$.

245 The CNTL simulation follows a trend commonly observed in atmospheric models, where the RH_i distribution peaks around $100\,\%$ before sharply declining due to rapid humidity quenching by ice growth schemes (Kärcher et al., 2023) or models using saturation adjustment schemes (Tompkins et al., 2007; Gierens et al., 2020). Unlike models employing a saturation adjustment, GEM's P3 microphysics scheme does not use such a constraint. When the depositional growth rate is reduced to $90\,\%$ (Dep_0.9) of the CNTL value, the RH_i distribution peak shifts from $100\,\%$ to $104\,\%$, and the maximum RH_i increases from $104\,\%$ to
250 $108\,\%$. Further reductions to $80\,\%$ (Dep_0.8) and $60\,\%$ (Dep_0.6) enhance moisture buildup, leading to higher RH_i maxima of $116\,\%$ and $128\,\%$, respectively, which align more closely with observations. However, these reductions also lower the distinct $100\,\%$ peak seen in the CNTL, suggesting a redistribution of humidity. The largest contributor to the underestimation is GEM's inability to capture the DTX sounding (Fig. B1).
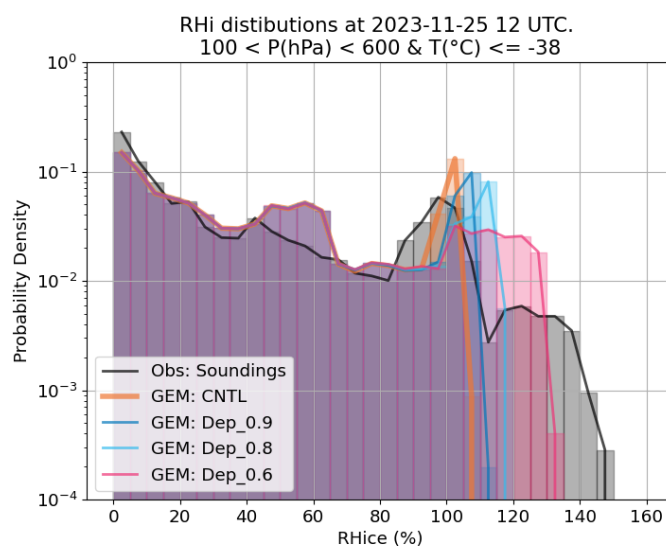
Figure 2. RHi distribution for CNTL, Dep_0.9, Dep_0.8 and Dep_0.6 simulations at 1200 UTC. The observations from all the radiosonde sounding is combined and shown as "Obs: Soundings" (black line). The GEM soundings include data in a 5 km × 5 km domain around the location of the balloon to account for uncertainty.

3.1.2 The outlier: DTX sounding

255 At the 500 hPa level, a deep trough was present over the Great Lakes region, indicating an area of lower pressure and cooler temperatures aloft (Fig. 1). This trough was associated with enhanced jet stream activity, which led to increased upper-level divergence. Such divergence promotes rising motion in the atmosphere, generating thin streaks of ice-supersaturated regions, which in turn favored cirrus cloud formation and the potential for persistent contrail development.

The DTX sounding profile reveals that the balloon drifted through one of these supersaturated streaks, recording RH_i val-
260 ues exceeding 140 % between 300 hPa and 200 hPa. While GEM accurately captured the broader upper-air trough, it failed to generate the highly ice-supersaturated regions above DTX (Fig. 3a). In contrast, most of the other stations, except for ALB, exhibited ice supersaturation between 400 hPa and 200 hPa, which GEM represented better (e.g., Fig. 3b). However, this improved representation may be due to the fact that the other soundings did not contain such thick layers of highly ice-supersaturated air, making them easier for the model to capture.

265 When the depositional growth rate is slowed the sensitivity simulations show a marginal improvement, with RHi values increasing to 106 % (Dep_0.9), 112 % (Dep_0.8), and 122 % (Dep_0.6). While this adjustment allows for a higher degree of ice supersaturation, the model still underestimates the extreme RHi values observed in the DTX sounding, where RHi exceeded 140 % (Fig. 3a). In comparison, the ice supersaturated regions are much better represented for the BUF sounding, especially in the Dep_0.8 and Dep_0.6 simulations. These slower deposition growth rates corresponds to α_d smaller than 0.1 for ice particle
270 diameters of larger than 50 μm (Fig. A1). There are very thin ice-supersaturated layers, such as at 220 hPa in Fig. 3b, which are not well represented in the GEM simulations. This discrepancy may be attributed to the vertical resolution of the model, where the layer thickness at this pressure level is approximately 250 m. The model's relatively coarse vertical resolution may smooth out small-scale supersaturation features, limiting its ability to resolve narrow layers of high RH_i observed in the soundings.
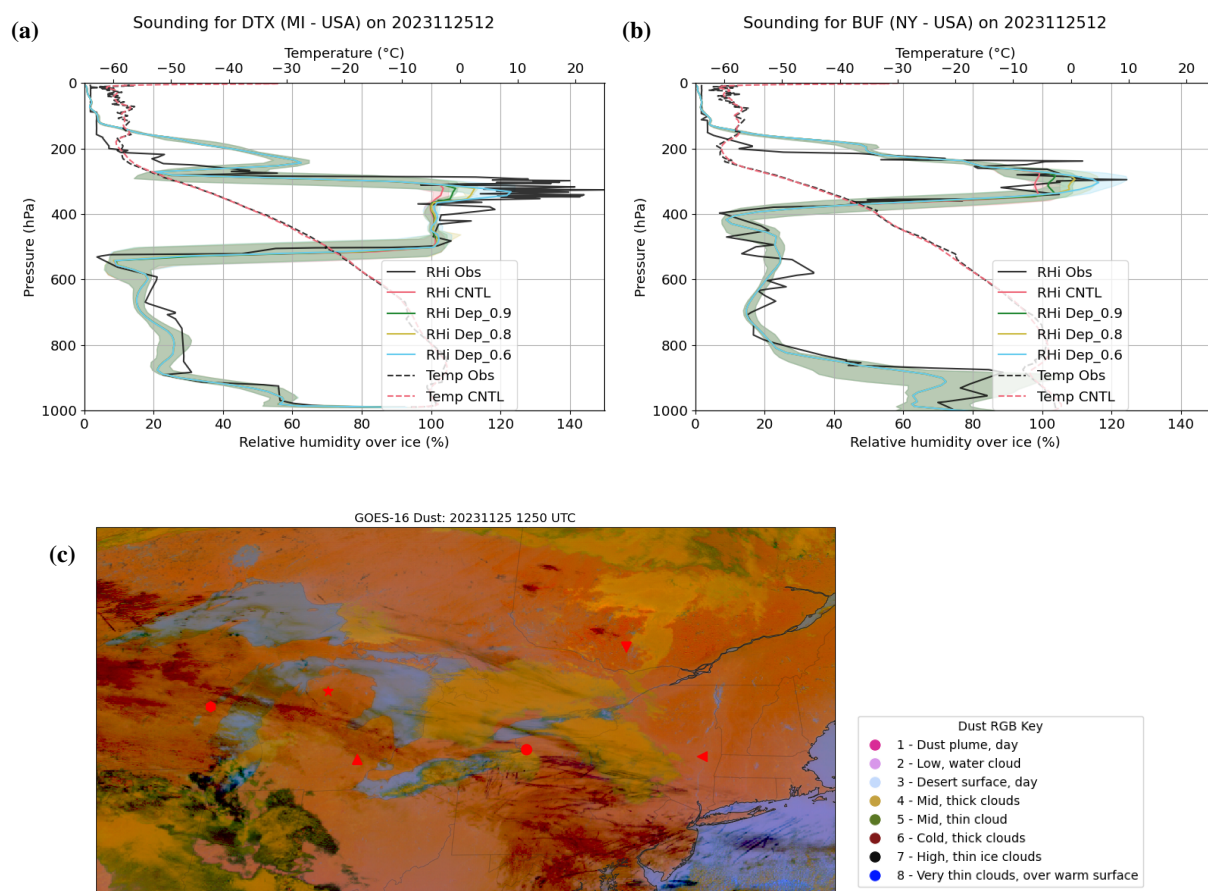
(a)

Sounding for DTX (MI - USA) on 2023112512

(b)

Sounding for BUF (NY - USA) on 2023112512

(c)

GOES-16 Dust: 20231125 1250 UTC

Figure 3. Soundings for **(a)** DTX, **(b)** BUF compared to the Dep_0.9, Dep_0.8 and Dep_0.6 simulations. The shaded areas are the minimum and maximum values for a 5 km × 5 km domain around the location of the balloon. Panel **(c)** is the GOES-16 Dust RGB at 1250 UTC

3.1.3 GEM vs ceilometer observations at CYYZ

In the Great Lakes region, the interaction between cold Arctic air masses and the relatively warmer lake waters frequently triggers lake-effect snow events (Niziol et al., 1995). The synoptic conditions on 25 Nov 2023 and the following days facilitated such phenomena, leading to the formation of low clouds and heavy snowfall in the surrounding areas. On this day, these low clouds significantly attenuated the ceilometer signal, making it nearly impossible to retrieve data from cirrus clouds between 1300 UTC and 1700 UTC. However, a descending high cloud base was still noticeable, aligning with the descending moist layer observed in all simulations (Fig. 5).

Between 1100 UTC and 1200 UTC, the ceilometer's backscatter intensity displayed a diffused structure, indicative of thin ice clouds like cirrus or contrails around ~ 10 km in altitude. By 1200 UTC to 1300 UTC, the cirrus clouds became more structured, with a lower cloud base near 8 km, suggesting the presence of ice-supersaturated regions. Figure 4 presents a time series of the RH$_i$ profiles for all simulations at the same location as the CYYX ceilometer. The Dep_0.8 and Dep_0.6 simulations support the presence of ice-supersaturated regions between 8 and 10 km and indicate the potential for persistent contrail formation around ~ 10 km.

From 1300 UTC until around 1500 UTC, all simulations except Dep_0.6 failed to indicate conditions suitable for persistent contrail formation. During this time, contrails were observed over Toronto, but images at 1420 UTC and simulations at 1400 UTC show no indication of new contrail formation, only widespread older contrails that had formed upstream towards the west.

Variations in the depositional growth rates of ice particles significantly affect the persistence and spatial extent of ice-supersaturated regions. While all sensitivity simulations indicate the presence of contrail-forming regions, the CNTL simulations exhibit conditions that are excessively dry prior to 1645 UTC. After this time, although ice-supersaturated regions persists above 6 km, the ambient temperature remains too elevated, warmer than $-45\,°C$, for the aircraft plume to achieve supersaturation. Consequently, the nucleation and freezing of water droplets, essential for contrail persistence in ice-supersaturated environments, are inhibited. In contrast, the reduced moisture deposition rate, synonymous to lower α_d values, in the sensitivity simulations allows for a more extensive and intense presence of ice-supersaturated regions, thereby enhancing the likelihood of persistent contrail formation.
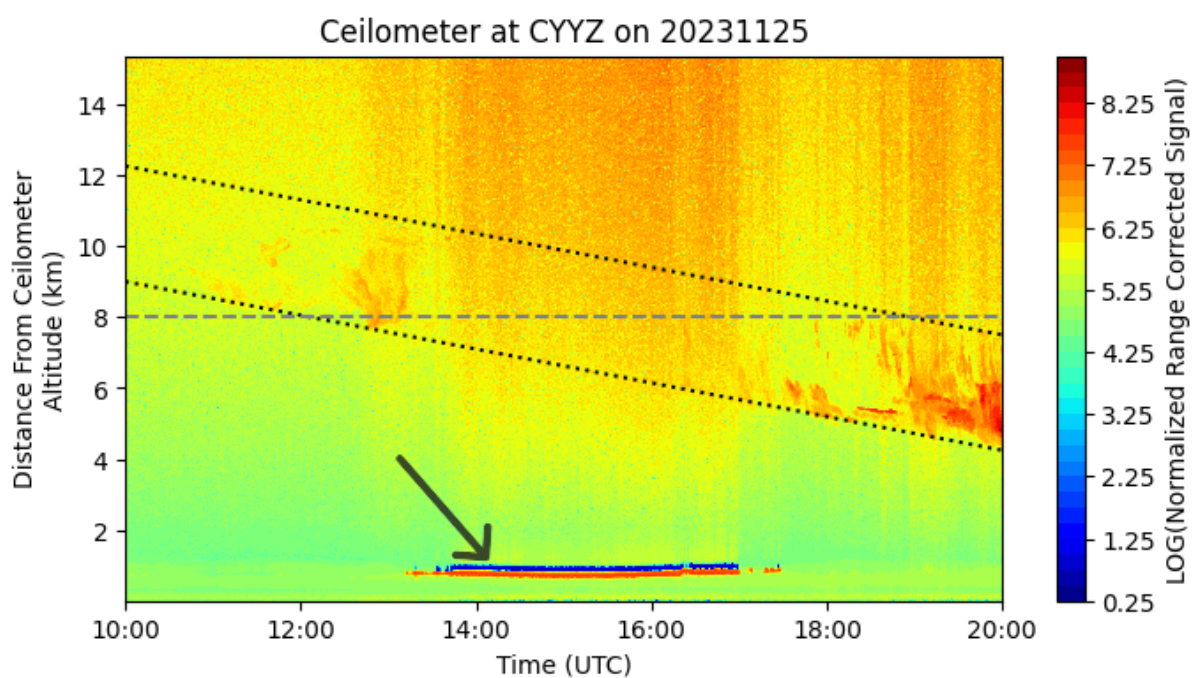
Figure 4. Time series of ceilometer backscatter profiles for 25 Nov 2023 at Pearson International Airport (CYYZ, Toronto). The dotted lines indicate the descending cloud bottom and cloud top over time. The dashed line shows the altitude of the cloud bottom at 1200 UTC. The arrow indicates the low-level stratus between 1300 UTC and 1700 UTC.
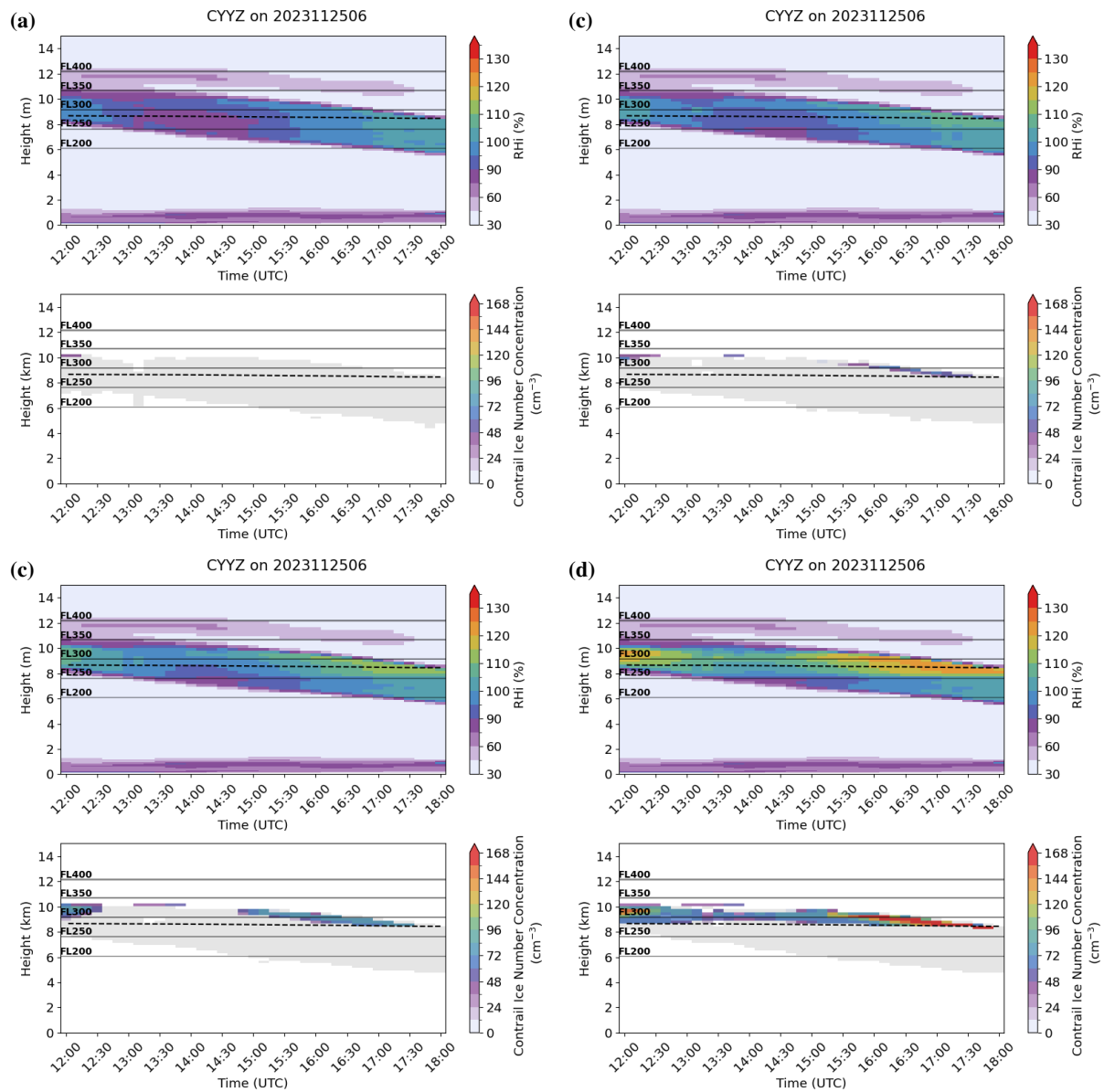
Figure 5. Time series for the RH_i for the **(a)** CNTL, **(b)** Dep_0.9, **(c)** Dep_0.8 and **(d)** Dep_0.6 simulations between 1200 UTC and 1800 UTC. The grey shaded areas are the ice number concentration from ice clouds in the model. The dotted line one the where the temperature is $-45\,°C$ and the solid grey lines are the flight levels (FL).

3.2 CoAT simulations

300 #### 3.2.1 Sounding vs CoAT

Here, we compare the atmospheric conditions at three sounding stations (ALB, BUF, and APX) spanning west to east along the main flight corridor at 1200 UTC. The sounding data provide input for the CoAT model, which determines the formation of persistent contrail regions and evaluates contrail properties, such as contrail depth and CINC that survive the wake vortex. These simulations are then compared to results where the simulated atmospheric conditions from GEM serve as input for 305 CoAT. For all comparisons, we assume the aircraft characteristics of an A321 and only consider the Dep_0.8 simulation.

Figure 6 illustrates that flights traveling between ALB and BUF will begin to encounter high ice clouds. At ALB, the upper atmosphere remains dry and is not conducive to cirrus or contrail formation (Fig. 6a). In contrast, at BUF, between 400 hPa and 200 hPa, the observed RH_i exhibits significant variability, with multiple layers exceeding 100 %, indicating the presence of ice-supersaturated regions. This is particularly pronounced between 300 hPa and 260 hPa, as well as in a very shallow layer 310 at 240 hPa, where RH_i frequently surpasses 100 %. In these regions, the ambient temperature is below the critical threshold for SAC, creating favorable conditions for persistent contrail formation (Fig. 6b).

While GEM generally captures the ice-supersaturated regions well, it does not fully resolve the magnitude of the observed supersaturation events, often smoothing out peaks where RH_i exceeds 100 %. This discrepancy suggests that accurately capturing thin ice-supersaturated layers requires higher vertical resolution in models. The presence of highly localized supersaturation 315 spikes (e.g. at 290 hPa) leads to CoAT generating deeper contrail depths and higher CINC of 310 m and 190 cm^{-3}, respectively, compared to GEM-CoAT, which produced contrail depths and CINC of 160 m $\in$ [100 m, 275 m] and 60 cm^{-3} $\in$ [58 cm^{-3}, 80 cm^{-3}], respectively (BUF, Fig. 6b).

It is important to note that in CoAT, SAC regions can be present even when the wake vortex model indicates no contrail formation (i.e., contrail depth and CINC of zero). This occurs because the wake vortex model accounts for adiabatic pro- 320 cesses during plume descent, where warming of the air leads to ice particle sublimation. In this case, despite a temperature of −52 °C and an RH_i of 102.5 % at a pressure of 270 hPa, all ice particles sublimated within the first few minutes of the young contrail's lifetime. This indicates that merely using SAC as an indicator for contrail persistence may overestimate the regions in which ice particles can survive the wake vortex dynamics.

In the case of the APX sounding (see Fig. 6c), the regions of supersaturation with respect to ice (SAC) appear to match 325 reasonably well between the observational data and the GEM-CoAT simulation. However, the figure indicates that GEM-CoAT predicts a higher and more vertically extensive RH_i from approximately 340 hPa to 240 hPa, compared to the narrower layer observed in the sounding data. As a result, GEM-CoAT overestimates both the contrail depth, generally simulating thicknesses between 250 m and 300 m, and the CINC. In contrast, CoAT typically shows contrail depths between 50 m and 100 m, except for one thin layer where the contrail depth reaches 225 m.

330 In general, an A321 aircraft operating along the ALB-BUF-APX corridor may have generated persistent contrails in the vicinity of the BUF and APX stations between 350 hPa and 250 hPa at 1200 UTC. Subsequently, at approximately 1300 UTC, flight DL384 traversed the Toronto region along the ALB-BUF-APX corridor at an altitude of ~300 hPa (30,000 ft). The

analysis of this specific flight path is superimposed on the output of the model simulations, with the potential for contrail
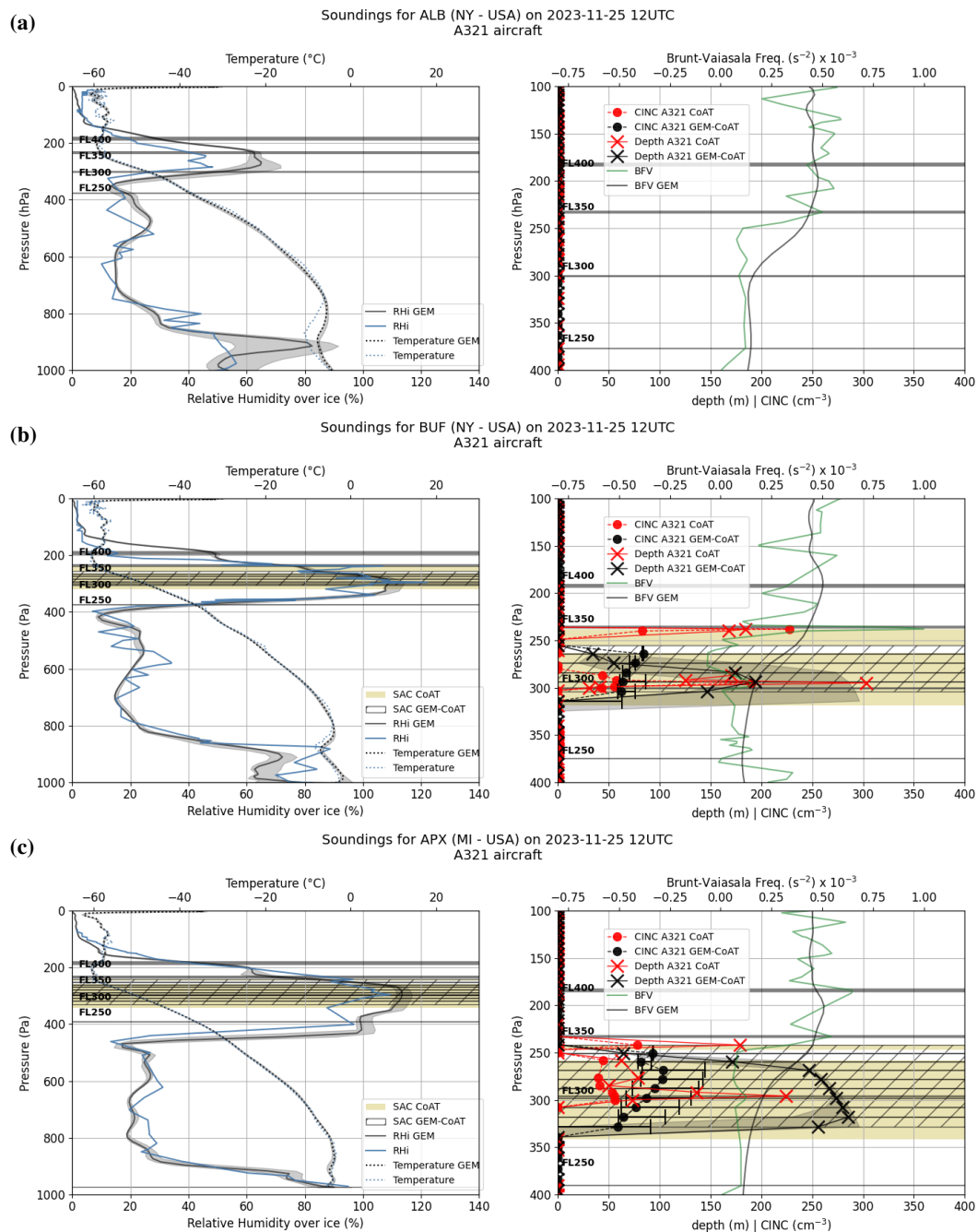
formation discussed in the following section.

Figure 6. Atmospheric soundings for **(a)** ALB, **(b)** BUF and **(c)** APX compared to the GEM-CoAT Dep_0.8 simulation. The shaded areas are the minimum and maximum values for a $5\,km \times 5\,km$ domain around the location of the balloon. The shaded yellow and hatched areas are where persistent contrails can form according to the Schmidt-Appelman Criterion (SAC) in CoAT (calculated using the sounding information) and GEM-CoAT (calculated using the model data), respectively. The grey lines are the flight levels (FL).

3.2.2 Superimposed cross-section flight track analysis

Figure 7 illustrates the simulated cross-sectional regions of persistent contrail formation, highlighting areas where ice particles survive the wake vortex along the A321 flight route. The aircraft, operating along the ALB-BUF-APX corridor, maintains an altitude of 300 hPa (30,000 ft) between $-74\,°W$ and $-84\,°W$ before ascending to 240 hPa (34,000 ft) at $-84\,°W$, where it continues cruising. Over this cross-section, the CoAT Dep_0.8 simulation predicts young contrails with a CINC mean [10th percentile, 90th percentile] of 83.9 cm^{-3} [62.8 cm^{-3}, 118.5 cm^{-3}] (Figure 7a and b).

During its cruise at 300 hPa, the A321 traverses regions favorable for contrail formation, particularly over Lake Ontario as it approaches the APX station. Observations from GOES-16 Dust imagery confirm the presence of multiple aircraft-generated contrails between 1300 UTC and 1500 UTC (Figure 1). Near the APX station, the A321 ascends out of the contrail-forming layer into a drier atmospheric region, where contrail formation ceases.

A comparison between the A321 Dep_0.8 (Figure 7b) and A321 CNTL (Figure 7d) reveals that the faster deposition growth simulation (CNTL) exhibits a lower mean CINC (64.6 cm^{-3}). This trend is further supported by the significantly lower CINC 10th percentile in the A321 CNTL simulation (5.6 cm^{-3}), indicating a shallower distribution of ice particles under faster depositional growth rates. The reduction in ice particle survival is attributed to the enhanced moisture depletion in the ice-supersaturated regions due to faster deposition, leading to a decrease in RH$_i$ and ultimately lowering the ice number survival fraction during the wake vortex phase (Figure 7a and c). Consequently, the A321 CNTL simulation produces shallower contrails (detailed in the appendix) with lower contrail ice concentrations compared to the Dep_0.8 simulation, impacting the contrail's lifetime and evolution.

When the A321 aircraft (medium-weight category) is replaced by a B747 (heavy-weight category) in the B747 Dep_0.8 and B747 CNTL simulations, stark differences emerge. The B747 CNTL simulation indicates a significant reduction in the contrail formation region, suggesting that heavy-weight category aircraft flying the same route and at the same time may form fewer or no contrails compared to the medium-weight category aircraft (Figure 7d and h). The deeper wake generated by the B747 results in increased adiabatic heating and reduced ice particle survival, leading to a mean CINC of only 14.3 cm^{-3} compared to 64.6 cm^{-3} for the A321 (Table 3). A similar, though less pronounced, reduction is observed between the B747 Dep_0.8 (61.1 cm^{-3}) and A321 Dep_0.8 (83.9 cm^{-3}) simulations.

These findings highlight the role that aircraft weight, especially at near ice-supersaturated conditions, and deposition growth rates play in simulating contrail formation and persistence accurately. While faster deposition reduces contrail ice concentrations, heavier aircraft further amplify this effect by increasing wake turbulence and adiabatic heating, ultimately limiting the conditions necessary for persistent contrails.

Table 3. Comparison of the Contrail Ice Number Concentration (CINC) and the Ice Particle Survival (IPS) mean, 10th and 90th percentiles for A321 Dep_0.8, A321 CNTL, B747 Dep_0.8, and B747 CNTL along the flight route in Figure 7.

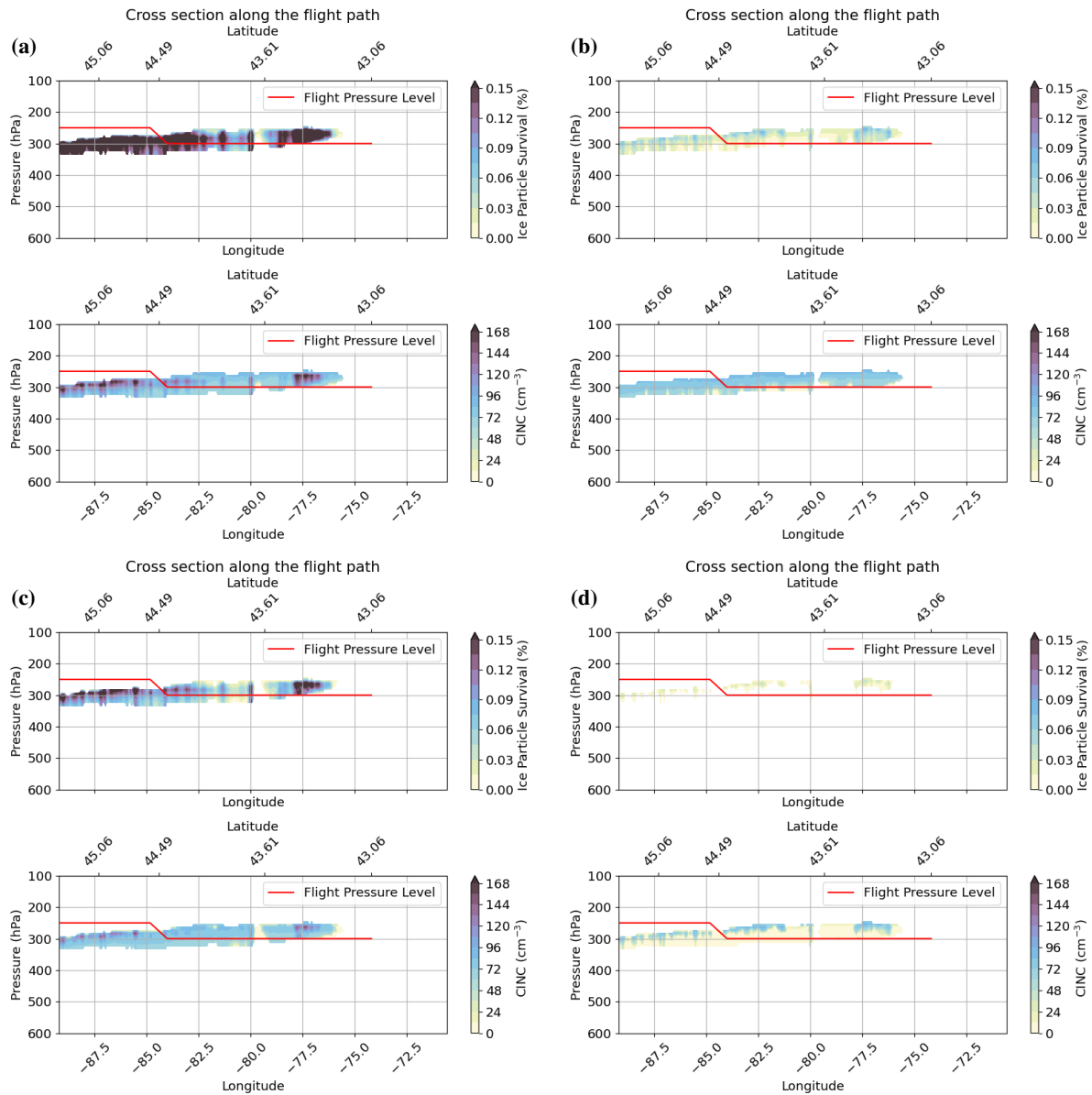| Parameter	A321 0.8_Dep	A321 CNTL	B747 0.8_Dep	B747 CNTL
CINC mean (cm^{-3})	83.9	64.6	61.1	14.3
CINC 10th (cm^{-3})	62.8	5.6	0.0	0.0
CINC 90th (cm^{-3})	118.4	87.8	88.3	65.8
IPS mean (%)	12.1	2.4	7.0	1.0
IPS 10th perc (%)	2.3	0.5	1.2	0.1
IPS 90th perc (%)	22.1	4.7	12.4	2.2

Figure 7. Vertical cross-section along the flight path (ALB-BUF-APX) for **(a)** DL384 Dep_0.8 (A321), **(b)** DL384 CNTL (A321), **(c)** DL384 Dep_0.8 (B747) and **(d)** DL384 Dep_0.8 (B747) overlaid over regions showing the ice particle survival and contrail ice number concentration at 1300 UTC.
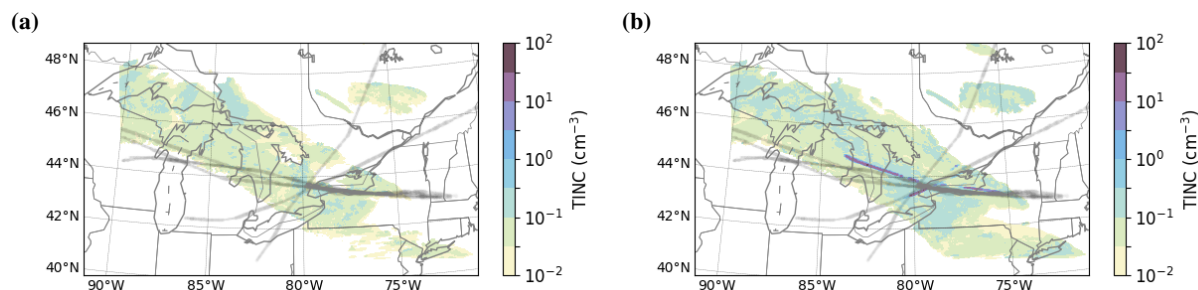
Figure 8. Combined ice number concentration from GEM-P3 nucleation scheme and the GEM-CoAT scheme. The maximum ice number concentration is selected between 320 hPa and 200 hPa and RH_i larger than 90 % and plotted. Flight information from Table 2 is used as input for the **(a)** CNTL and **(b)** Dep_0.8 simulations at 1420 UTC. The flight tracks are shown in grey lines.

3.2.3 Contrail simulations in GEM-CoAT

365 In this section, we incorporate the flight information into GEM-CoAT using the aircraft characteristics listed in Table 2. We simulate contrail formation based on the variation of aircraft properties and flight routes.

From the GOES-16 observations and photographs (Fig. 1), it is evident that multiple aircraft-generated contrails were present over the Toronto area at 1420 UTC. Contrail formation began around 1200 UTC, increasing in extent and number until 1600 UTC. Here, we analyze the simulated contrails formed by three specific aircraft: TK6061 (B747), DL384 (A321),

370 and CV6686 (B747). The CINC produced by these aircraft is combined with the ice number concentration (INC) generated by GEM-P3's nucleation schemes, to get the total ice number concentration (TINC), before being advected. The simulated contrails are then compared with GOES-16 Dust observations at 1420 UTC. Figure 8a highlights the limitation of using standard depositional growth rates, as the CNTL simulation fails to reproduce any contrails over the domain at any time. Instead, it only represents INC from GEM-P3's ice nucleation scheme. In contrast, the Dep_0.8 simulation successfully captures contrail

375 formation, particularly from the TK6061 and DL384 aircraft, which were flying at flight levels FL310 and FL300, respectively (Fig. 8b and Table 2). These aircraft overflew Toronto at 1345 UTC and 1245 UTC, respectively, while BUF soundings at 1200 UTC indicated persistent contrail formation regions between FL290 and FL330 (Fig. 3b). Additionally, CV6686 briefly formed a contrail north of Toronto, which dissipated within an hour due to its altitude at FL340, where it flew in and out of an ice-supersaturated layer. The locations of these simulated contrails from these aircraft align well with the contrails detected by

380 GOES-16 Dust observations, a result that is only achieved when depositional growth rates are slowed.

4 Summary and conclusions

On 25 November 2023, between 1200 UTC and 1800 UTC, widespread ice-supersaturated regions formed, resulting in a high occurrence of contrail formation over eastern Canada and the USA. Photographic images from Toronto and satellite-based observations from the GOES-16 Advanced Baseline Imager Dust Red-Green-Blue composite indicated that aviation contrails

385   persisted for several hours, especially over the Lake Ontario region. Ceilometer data taken from Toronto Pearson International Airport (CYYZ), radiosonde soundings from Albany, Gaylord, Buffalo, White Lake, Green Bay, International Falls, Maniwaki, and Pickle Lake were used to analyze the atmospheric conditions under which the ice-supersaturated regions formed.

The Global Environmental Multiscale (GEM) model, which includes the Predicted Particle Properties (P3) microphysics scheme was employed as the base model for high-resolution simulations. The Contrail Avoidance Tool (CoAT), which consists

390   of Schmidt-Appleman Criteria (SAC) and the wake vortex model from, was used to determine persistent contrail forming regions and contrail properties.

First, we analyzed the ability of GEM-P3 to simulate ice-supersaturated regions by heuristically adjusting the depositional growth rate of ice particles and to compare it against the CNTL simulation, where no reduction factor was applied. The findings can be summarized as follows:

395   – The CNTL simulation underestimates RH_i distribution, following a common trend in atmospheric models in which the moisture is quenched too quickly, resulting in a RH_i peak of $\sim$100 %.

   – Sensitivity simulations indicate that reductions in ice particle depositional growth rates enhances moisture buildup, leading to improved forecasts of RH_i influencing the extent of contrail forming regions.

   – In CoAT, the presence of persistent contrail forming regions (SAC) does not necessarily imply contrail formation, as

400   wake vortex dynamics can induce adiabatic warming during plume descent, leading to complete ice particle sublimation despite favorable thermodynamic conditions. This suggests that SAC alone may overestimate the spatial extent of persistent contrail regions.

Second, the CoAT model was employed to simulate regions of persistent contrail formation and associated microphysical properties for two aircraft types: the A321 (medium-weight) and the B747 (heavy-weight), along the ALB-BUF-APX flight

405   corridor. The key findings are summarized as follows:

   – In the Dep_0.8 simulations, the B747 induces deeper wake vortices, leading to enhanced adiabatic heating and a subsequent 27 % reduction in mean contrail ice number concentrations relative to the A321.

   – In the CNTL simulations, this reduction is even more pronounced at 78%, suggesting that heavier aircraft may significantly inhibit contrail formation under similar atmospheric conditions due to increased wake turbulence and ice particle

410   sublimation.

These results underscore the critical influence of aircraft-specific characteristics on contrail formation and persistence. More importantly, they demonstrate that with a reduced depositional growth rate of ice particles, the GEM-CoAT model was able

to reproduce the observed contrails.This highlights the need to accurately represent ice supersaturation processes in numerical simulations to improve the fidelity of contrail modeling.

415

In this context, recent work on the introduction of the 3-moment treatment of ice in P3 by Milbrandt et al. (2021) has advanced the representation of microphysical processes, with P3 now fully 3-moment for all ice-related processes (Morrison et al., 2025). This allows the shape parameter of the ice size distribution, which is proportional to the relative spectral dispersion, to evolve independently for all processes, including depositional growth. As a result, the deposition rate both influences and is

420   influenced by the shape parameter. Incorporating these interactions should, in principle, lead to improved representation of ice-supersaturated regions in the upper troposphere within GEM-P3. The underestimation of ice supersaturation in models can be attributed to limitations in their representation of phase relaxation, turbulence, and layer resolution. Korolev and Mazin (2003) shows the important role of phase relaxation in regulating supersaturation within ice clouds. In typical cirrus conditions, where the ice crystal number concentration and size are approximately $20\,\mathrm{cm}^{-3}$ and $0.2\,\mathrm{\mu m}$, respectively (Lohmann et al., 2016), the

425   phase relaxation timescale is around $200\,\mathrm{s}$. These timescales can range between $60\,\mathrm{s}$ and $460\,\mathrm{s}$ in cirrus clouds, exceeding the timesteps commonly used in models. The substantially longer phase relaxation timescales allow supersaturation to persist beyond what is typically represented in numerical models. Our CNTL simulation in GEM-P3 is unable to reproduce the buildup of supersaturation while using a $30\,\mathrm{s}$ model timestep, unless the ice deposition growth rate is adjusted. A limitation in the P3 microphysics scheme used in this study is its treatment of ice nucleation. While the scheme has undergone several improve-

430   ments, the deposition nucleation process forms ice even at temperatures colder than $-38\,°\mathrm{C}$, for which it was not originally designed. Additionally, the ice nucleation rate is currently set to $0.1\,\mathrm{cm}^{-3}\mathrm{s}^{-1}$, resulting in ice relaxation timescales of approximately $340\,\mathrm{s}$, toward the lower end of the range associated with cirrus clouds. This may contribute to the model's inability to sustain elevated supersaturation levels. Ongoing work aims to refine the representation of ice nucleation at temperatures below $-38\,°\mathrm{C}$, following approaches similar to those of Gasparini et al. (2025).

435   Another factor influencing the underestimation of ice supersaturation is the vertical grid spacing. Many global and regional climate models employ relatively coarse vertical layers, which limit their ability to resolve fine-scale turbulence and small-scale vertical motions that sustain localized supersaturation events. In coarse-resolution models, turbulence-induced variations in humidity tend to be smoothed out, leading to an under representation of extreme supersaturation values (Burkhardt and Kärcher, 2009). This limitation becomes more pronounced when the Richardson number exceeds 0.25, which represents the

440   ratio of buoyant energy to shear kinetic energy and determines the dynamic stability of the atmosphere (Stull, 2016). In such cases, significant wind shear within well-stratified layers can reduce the persistence of supersaturated regions (Thompson et al., 2024). Although GEM-P3 employs a vertical grid spacing of $230\,\mathrm{m}$ in the upper atmosphere, our CNTL simulations cannot reproduce the very shallow layers of elevated $\mathrm{RH_i}$. This suggests that even relatively high-resolution models may struggle to capture the fine-scale structure of supersaturation layers, potentially contributing to the underestimation bias.

445

Code and data availability. Code will be made available after acceptance but can be showed to reviewers if desired. All data including those used to initialize the simulations, the simulated outputs, used in this study are archived internally for 5-year at the Canadian Meteorological Centre. The plotting software, GEM settings files and CoAT source code can be found at https://doi.org/10.5281/zenodo.15611592. The ceilometer and sounding data (University of Wyoming web site, http://weather.uwyo.edu/) can be found at https://doi.org/10.5281/zenodo.15643030.

Appendix A

A1   Depositional growth of ice particles

$$\frac{dm}{dt} = \frac{4\pi C(S_{v,i} - 1)}{\frac{\rho_i RT}{e_{\text{sat},i} D'_v M_w} + \frac{L_s \rho_i}{k'_a T}\left(\frac{L_s M_w}{RT} - 1\right)}, \tag{A1}$$

The equation describes the rate of mass growth of an ice particle, governed by the balance of vapor diffusion and heat conduction. The terms include the geometric capacitance C, supersaturation over ice $S_{v,i}$, ice density ρ_i, and saturation vapor pressure over ice $e_{\text{sat},i}$, along with the universal gas constant R, absolute temperature T, and water's molar mass M_w. The latent heat of sublimation L_s, thermal conductivity k'_a, and modified vapor diffusivity D'_v account for heat and mass transfer limitations in the crystal's growth process (Pruppacher and Klett, 2010).

$$D'_v = \frac{D_v}{\frac{r}{r+\Delta_v} + \frac{D_v}{r\alpha_D}\sqrt{\frac{2\pi M_w}{RT_s}}}, \tag{A2}$$

This correction to the standard diffusivity D_v incorporates only the kinetic effects and excludes ventilation, which is negligible for small ice crystals and thus disregarded (Pruppacher and Klett, 2010; Gierens et al., 2003). The key parameters in the kinetic correction factor include the crystal radius r and the "jump" distance Δ_v, typically set equal to the molecular mean free path. T_s represents the surface temperature of the growing ice crystal, and α_D is the deposition coefficient. α_D is defined via the transcendental equation:

$$\alpha_d = \left(\frac{s_{\text{sfc},d}}{s_{\text{crit}}}\right)^b \tanh\left[\left(\frac{s_{\text{crit}}}{s_{\text{sfc},d}}\right)^b\right] \tag{A3}$$

which determines how efficiently water vapor deposits onto ice crystals. It depends on the local ice supersaturation at the crystal surface $s_{\text{sfc},d}$, the critical supersaturation s_{crit}, and a growth mechanism parameter b, which controls the transition between different crystal growth modes. The ice supersaturation $s_{\text{sfc},d}$ (Lamb and Verlinde, 2011) at the ice crystal surface and the supercooling function s_{crit} based on the analysis of Zhang and Harrington (2014) and used by Kärcher et al. (2023)

$$s_{\text{sfc},d} = s\left(1 + \frac{\alpha_d r}{\ell}\right)^{-1}, \quad s_{\text{crit}}[\%] = 0.019655 \cdot (\Delta T[K])^{1.4305} \tag{A4}$$

where s is the ambient supersaturation and ℓ the diffusion length. Similar to Kärcher et al. (2023) we define the transition growth regime with a size-dependent growth parameter m for spherical ice crystals:

$$b = \begin{cases} 1, & r < 10\mu m \\ 1 + 14\left(\frac{r - 10\mu m}{70\mu m - 10\mu m}\right), & 10\mu m \leq r \leq 70\mu m \\ 15, & r > 70\mu m \end{cases} \tag{A5}$$
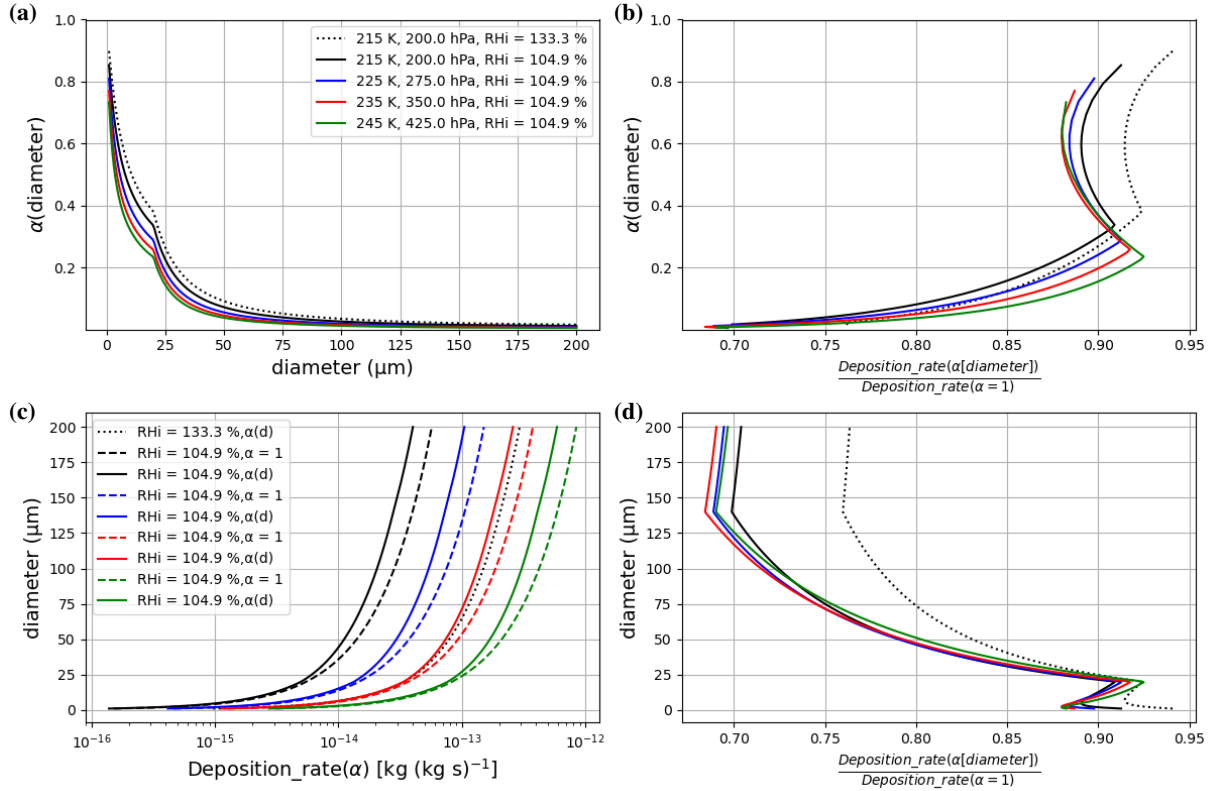
27

Figure A1. (a) The deposition growth coefficient (α_D) as a function of ice particle diameter, **(b)** relationship between α_D and the normalized deposition rate at $\alpha_D = 1$, **(c)** deposition rate as a function of α_D and **(d)** the ice particle diameter dependence on the normalized deposition rate under varying atmospheric conditions.

In P3, the growth of ice particles follows the same formulation as in equation A1, but instead of using D'_v, the uncorrected diffusivity is used D_v, which is a function of temperature T and pressure P (Hall and Pruppacher, 1976). Consequently, we do not have an explicit description for α_D that can be directly modified to determine the depositional growth rate.

To address this, we solved for α_D for ice crystal sizes between 1 and 200 µm using the Newton-Raphson method, an iterative numerical technique for finding the root of a nonlinear equation and making an initial guess for $\alpha_D = 0.1$ (equations A3 and A4). The computed α_D values were then compared to a reference case where $\alpha_D = 1$, allowing us to evaluate the ratio between $\left(\frac{dm}{dt}\right)_{\alpha_D}$ and $\left(\frac{dm}{dt}\right)_{\alpha_D=1}$.

As shown in Figure A1, this ratio, referred to as the reduction factor for the depositional growth rate, ranges between 0.65 and 0.95 (Fig. A1). Therefore, we implemented reduction factors of 0.6 (Dep_0.6), 0.8 (Dep_0.8) and 0.9 (Dep_0.9) in our sensitivity simulations and compared them to the reference case (CNTL) where $\left(\frac{dm}{dt}\right)_{\alpha_D} = \left(\frac{dm}{dt}\right)_{\alpha_D=1}$.

A2 Contrail spread over multiple vertical levels

The fractional distributions, f_{r1} and f_{r2}, represent how the contrail ice is spread over multiple model levels. Specifically, f_{r1}

485 is the fraction of contrail ice within the current model level, while f_{r2} accounts for the fraction extending beyond the current level into a lower model layer. These fractions are computed using the depth of the contrail ($\text{Cd}(k)$) and the depth of the model level ($\text{Zd}(k)$).

The total ice crystal number and ice crystal mass concentrations in a grid box are denoted by $N_{i_{\text{tot}}}(k)$ and $Q_{i_{\text{tot}}}(k)$, respectively. These quantities are updated by adding the contributions from contrail ice ($N_{i_{\text{contrail}}}(k)$ and $Q_{i_{\text{contrail}}}(k)$) scaled by

490 the fractional distribution f_{r1}. Similarly, the ice content and ice crystals in the level below the current one, represented by $N_{i_{\text{tot}}}(k-1)$ and $Q_{i_{\text{tot}}}(k-1)$, are updated based on the portion of contrail ice extending downward, governed by f_{r2}.

$$f_{r1} = \frac{\text{Zd}(k)}{\text{Cd}(k)}, \qquad f_{r2} = \frac{\text{Cd}(k) - \text{Zd}(k)}{\text{Cd}(k)} \tag{A6}$$

$$N_{i_{\text{tot}}}(k) = N_{i_{\text{tot}}}(k) + N_{i_{\text{contrail}}}(k) \cdot f_{r1}, \qquad Q_{i_{\text{tot}}}(k) = Q_{i_{\text{tot}}}(k) + Q_{i_{\text{contrail}}}(k) \cdot f_{r1} \tag{A7}$$

$$N_{i_{\text{tot}}}(k-1) = N_{i_{\text{tot}}}(k-1) + N_{i_{\text{contrail}}}(k) \cdot f_{r2}, \qquad Q_{i_{\text{tot}}}(k-1) = Q_{i_{\text{tot}}}(k-1) + Q_{i_{\text{contrail}}}(k) \cdot f_{r2} \tag{A8}$$

495 ## Appendix B

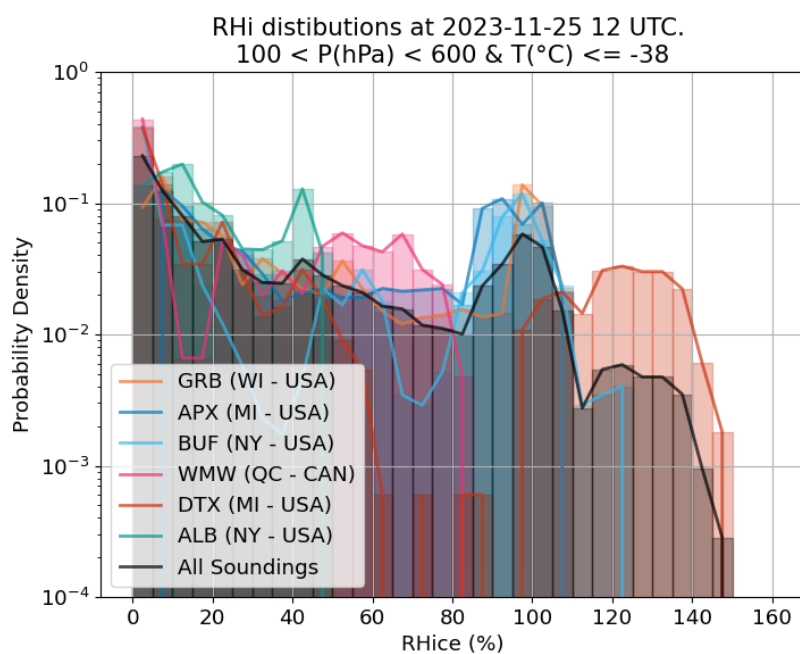### B1 Relative humidity distribution for radiosonde stations

Figure B1. Relative humidity with respect to ice distribution for all the radiosonde stations. The distributions only include data between pressures of 600 hPa and 100 hPa, and temperatures colder than $-38\,°C$.

Author contributions. ZD conducted the simulations and analyzed the results. ZD was the main author of the paper. AK, JM, ZD contributed to the study's design and the analysis of the results. All authors contributed to the study's writing.

Competing interests. The authors declare that they have no conflict of interest.

References

Blaylock, B. K.: GOES-2-go: Download and display GOES-East and GOES-West data (Version 2022.07.15), https://github.com/blaylockbk/

505   goes2go, 2023.

Burkhardt, U. and Kärcher, B.: Process-based simulation of contrail cirrus in a global climate model, Journal of Geophysical Research: Atmospheres, 114, https://doi.org/10.1029/2008JD011491, 2009.

Burkhardt, U. and Kärcher, B.: Global radiative forcing from contrail cirrus, Nature Climate Change, 1, 54–58, https://doi.org/10.1038/nclimate1068, publisher: Nature Publishing Group, 2011.

510   Burkhardt, U., Bock, L., and Bier, A.: Mitigating the contrail cirrus climate impact by reducing aircraft soot number emissions, Climate and Atmospheric Science, 1, 1–7, https://doi.org/10.1038/s41612-018-0046-4, 2018.

Cholette, M., Milbrandt, J. A., Morrison, H., Kirk, S., and Lalonde, L.-: Secondary Ice Production Improves Simulations of Freezing Rain, Geophysical Research Letters, 51, e2024GL108 490, https://doi.org/10.1029/2024GL108490, 2024.

Côté, J., Gravel, S., Méthot, A., Patoine, A., Roch, M., and Staniforth, A.: The Operational CMC–MRB Global Environmental Multiscale

515   (GEM) Model. Part I: Design Considerations and Formulation, Monthly Weather Review, 126, 1373–1395, https://doi.org/10.1175/1520-0493(1998)126<1373:TOCMGE>2.0.CO;2, 1998.

Flightradar24: Live Flight Tracker - Real-Time Flight Tracker Map, https://www.flightradar24.com/, 2024.

Fukuta, N. and Takahashi, T.: The Growth of Atmospheric Ice Crystals: A Summary of Findings in Vertical Supercooled Cloud Tunnel Studies, https://journals.ametsoc.org/view/journals/atsc/56/12/1520-0469_1999_056_1963_tgoaic_2.0.co_2.xml, section: Journal of the

520   Atmospheric Sciences, 1999.

Gasparini, B., Atlas, R., Voigt, A., Krämer, M., and Blossey, P. N.: Tropical cirrus evolution in a km-scale model with improved ice microphysics, EGUsphere, pp. 1–34, https://doi.org/10.5194/egusphere-2025-203, publisher: Copernicus GmbH, 2025.

Gierens, K., Matthes, S., and Rohs, S.: How Well Can Persistent Contrails Be Predicted?, Aerospace, 7, 169, https://doi.org/10.3390/aerospace7120169, 2020.

525   Gierens, K. M., Monier, M., and Gayet, J.-F.: The deposition coefficient and its role for cirrus clouds, Journal of Geophysical Research: Atmospheres, 108, https://doi.org/10.1029/2001JD001558, 2003.

Girard, C., Plante, A., Desgagné, M., McTaggart-Cowan, R., Côté, J., Charron, M., Gravel, S., Lee, V., Patoine, A., Qaddouri, A., Roch, M., Spacek, L., Tanguay, M., Vaillancourt, P. A., and Zadra, A.: Staggered Vertical Discretization of the Canadian Environmental Multiscale (GEM) Model Using a Coordinate of the Log-Hydrostatic-Pressure Type, Monthly Weather Review, 142, 1183–1196,

530   https://doi.org/10.1175/MWR-D-13-00255.1, 2014.

Hall, W. D. and Pruppacher, H. R.: The Survival of Ice Particles Falling from Cirrus Clouds in Subsaturated Air, Journal of the Atmospheric Sciences, 33, 1995–2006, https://doi.org/10.1175/1520-0469(1976)033<1995:TSOIPF>2.0.CO;2, 1976.

Harrington, J. Y. and Pokrifka, G. F.: An Approximate Criterion for Morphological Transformations in Small Vapor Grown Ice Crystals, https://doi.org/10.1175/JAS-D-23-0131.1, section: Journal of the Atmospheric Sciences, 2024.

535   Jensen, E. J., Kärcher, B., Woods, S., Krämer, M., and Ueyama, R.: The Impact of Gravity Waves on the Evolution of Tropical Anvil Cirrus Microphysical Properties, Journal of Geophysical Research: Atmospheres, 129, e2023JD039 887, https://doi.org/10.1029/2023JD039887, 2024.

Kalluri, S., Alcala, C., Carr, J., Griffith, P., Lebair, W., Lindsey, D., Race, R., Wu, X., and Zierk, S.: From Photons to Pixels: Processing Data from the Advanced Baseline Imager, Remote Sensing, 10, 177, https://doi.org/10.3390/rs10020177, 2018.

540   Korolev, A., Qu, Z., Milbrandt, J., Heckman, I., Cholette, M., Wolde, M., Nguyen, C., McFarquhar, G. M., Lawson, P., and Fridlind, A. M.:
          High ice water content in tropical mesoscale convective systems (a conceptual model), Atmospheric Chemistry and Physics, 24, 11 849–
          11 881, https://doi.org/10.5194/acp-24-11849-2024, 2024.

       Korolev, A. V. and Mazin, I. P.: Supersaturation of Water Vapor in Clouds, Journal of the Atmospheric Sciences, 60, 2957–2974,
          https://doi.org/10.1175/1520-0469(2003)060<2957:SOWVIC>2.0.CO;2, 2003.

545   Kärcher, B.: Formation and radiative forcing of contrail cirrus, Nature Communications, 9, 1824, https://doi.org/10.1038/s41467-018-04068-
          0, 2018.

       Kärcher, B., Jensen, E. J., Pokrifka, G. F., and Harrington, J. Y.: Ice Supersaturation Variability in Cirrus Clouds: Role
          of Vertical Wind Speeds and Deposition Coefficients, Journal of Geophysical Research: Atmospheres, 128, e2023JD039 324,
          https://doi.org/10.1029/2023JD039324, 2023.

550   Lamb,   D.   and   Verlinde,   J.:   Physics   and   Chemistry   of   Clouds,   Cambridge   University   Press,   Cambridge,
          https://doi.org/10.1017/CBO9780511976377, 2011.

       Lamb, K. D., Harrington, J. Y., Clouser, B. W., Moyer, E. J., Sarkozy, L., Ebert, V., Möhler, O., and Saathoff, H.: Re-evaluating cloud
          chamber constraints on depositional ice growth in cirrus clouds – Part 1: Model description and sensitivity tests, Atmospheric Chemistry
          and Physics, 23, 6043–6064, https://doi.org/10.5194/acp-23-6043-2023, publisher: Copernicus GmbH, 2023.

555   Lee, D. S., Fahey, D. W., Forster, P. M., Newton, P. J., Wit, R. C. N., Lim, L. L., Owen, B., and Sausen, R.: Aviation and global climate
          change in the 21st century, Atmospheric Environment, 43, 3520–3537, https://doi.org/10.1016/j.atmosenv.2009.04.024, 2009.

       Lee, D. S., Fahey, D. W., Skowron, A., Allen, M. R., Burkhardt, U., Chen, Q., Doherty, S. J., Freeman, S., Forster, P. M., Fuglestvedt, J.,
          Gettelman, A., De León, R. R., Lim, L. L., Lund, M. T., Millar, R. J., Owen, B., Penner, J. E., Pitari, G., Prather, M. J., Sausen, R., and
          Wilcox, L. J.: The contribution of global aviation to anthropogenic climate forcing for 2000 to 2018, Atmospheric Environment, 244,
560   117 834, https://doi.org/10.1016/j.atmosenv.2020.117834, 2021.

       Lee, D. S., Allen, M. R., Cumpsty, N., Owen, B., Shine, K. P., and Skowron, A.: Uncertainties in mitigating aviation non-
          CO 2 emissions for climate and air quality using hydrocarbon fuels, Environmental Science: Atmospheres, 3, 1693–1740,
          https://doi.org/10.1039/D3EA00091E, 2023.

       Lewellen, D. C. and Lewellen, W. S.: The Effects of Aircraft Wake Dynamics on Contrail Development, Journal of the Atmospheric Sciences,
565   58, 390–406, https://doi.org/10.1175/1520-0469(2001)058<0390:TEOAWD>2.0.CO;2, publisher: American Meteorological Society Sec-
          tion: Journal of the Atmospheric Sciences, 2001.

       Lewellen, D. C., Meza, O., and Huebsch, W. W.: Persistent Contrails and Contrail Cirrus. Part I: Large-Eddy Simulations from Inception to
          Demise, Journal of Atmospheric Sciences, 71, 4399–4419, https://doi.org/10.1175/JAS-D-13-0316.1, 2014.

       Lohmann, U., Lüönd, F., and Mahrt, F.: An introduction to clouds: From the Microscale to climate, Cambridge University Press,
570   https://doi.org/10.1017/CBO9781139087513, 2016.

       Lottermoser, A. and Unterstraßer, S.: High-resolution modelling of early contrail evolution from hydrogen-powered aircraft, EGUsphere, pp.
          1–33, https://doi.org/10.5194/egusphere-2024-3859, publisher: Copernicus GmbH, 2025.

       Milbrandt, J. A. and Morrison, H.: Parameterization of Cloud Microphysics Based on the Prediction of Bulk Ice Particle Properties. Part III:
          Introduction of Multiple Free Categories, Journal of Atmospheric Sciences, 73, 975–995, https://doi.org/10.1175/JAS-D-15-0204.1, 2016.

575   Milbrandt, J. A., Bélair, S., Faucher, M., Vallée, M., Carrera, M. L., and Glazer, A.: The Pan-Canadian High Resolution (2.5 km) Deterministic
          Prediction System, Weather and Forecasting, 31, 1791–1816, https://doi.org/10.1175/WAF-D-16-0035.1, 2016.

Milbrandt, J. A., Morrison, H., Ii, D. T. D., and Paukert, M.: A Triple-Moment Representation of Ice in the Predicted Particle Properties (P3) Microphysics Scheme, Journal of the Atmospheric Sciences, 78, 439–458, https://doi.org/10.1175/JAS-D-20-0084.1, 2021.

580 Morrison, H. and Milbrandt, J. A.: Parameterization of Cloud Microphysics Based on the Prediction of Bulk Ice Particle Properties. Part I: Scheme Description and Idealized Tests, Journal of the Atmospheric Sciences, 72, 287–311, https://doi.org/10.1175/JAS-D-14-0065.1, publisher: American Meteorological Society Section: Journal of the Atmospheric Sciences, 2015.

Morrison, H., Milbrandt, J. A., and Cholette, M.: A Complete Three-Moment Representation of Ice in the Predicted Particle Properties (P3) Microphysics Scheme, Journal of Advances in Modeling Earth Systems, 17, e2024MS004 644, https://doi.org/10.1029/2024MS004644, 2025.

585 Niziol, T. A., Snyder, W. R., and Waldstreicher, J. S.: Winter Weather Forecasting throughout the Eastern United States. Part IV: Lake Effect Snow, https://journals.ametsoc.org/view/journals/wefo/10/1/1520-0434_1995_010_0061_wwftte_2_0_co_2.xml, section: Weather and Forecasting, 1995.

Pruppacher, H. R. and Klett, J. D.: Microphysics of Clouds and Precipitation, Atmospheric and Oceanographic Sciences Library, Springer Netherlands, 2 edn., 2010.

590 Qu, Z., Korolev, A., Milbrandt, J. A., Heckman, I., Huang, Y., McFarquhar, G. M., Morrison, H., Wolde, M., and Nguyen, C.: The impacts of secondary ice production on microphysics and dynamics in tropical convection, Atmospheric Chemistry and Physics, 22, 12 287–12 310, https://doi.org/10.5194/acp-22-12287-2022, 2022.

Schumann, U.: On conditions for contrail formation from aircraft exhausts, Meteorologische Zeitschrift, pp. 4–23, https://doi.org/10.1127/metz/5/1996/4, publisher: Schweizerbart'sche Verlagsbuchhandlung, 1996.

595 Schumann, U.: A contrail cirrus prediction model, Geoscientific Model Development, 5, 543–580, https://doi.org/10.5194/gmd-5-543-2012, 2012.

Seidel, D. J., Sun, B., Pettey, M., and Reale, A.: Global radiosonde balloon drift statistics, Journal of Geophysical Research: Atmospheres, 116, https://doi.org/10.1029/2010JD014891, 2011.

Sperber, D. and Gierens, K.: Towards a more reliable forecast of ice supersaturation: concept of a one-moment ice-cloud scheme that avoids 600 saturation adjustment, Atmospheric Chemistry and Physics, 23, 15 609–15 627, https://doi.org/10.5194/acp-23-15609-2023, 2023.

Stull, R.: Practical Meteorology: An Algebra-based Survey of Atmospheric Science, AVP International, University of British Columbia, google-Books-ID: xP2sDAEACAAJ, 2016.

Sussmann, R. and Gierens, K. M.: Lidar and numerical studies on the different evolution of vortex pair and secondary wake in young contrails, Journal of Geophysical Research Atmospheres, 104, 2131–2142, https://doi.org/10.1029/1998JD200034, 1999.

605 Teoh, R., Schumann, U., Majumdar, A., and Stettler, M. E. J.: Mitigating the Climate Forcing of Aircraft Contrails by Small-Scale Diversions and Technology Adoption, Environmental Science & Technology, 54, 2941–2950, https://doi.org/10.1021/acs.est.9b05608, 2020.

Teoh, R., Schumann, U., Gryspeerdt, E., Shapiro, M., Molloy, J., Koudis, G., Voigt, C., and Stettler, M. E. J.: Aviation contrail climate effects in the North Atlantic from 2016 to 2021, Atmospheric Chemistry and Physics, 22, 10 919–10 935, https://doi.org/10.5194/acp-22-10919-2022, publisher: Copernicus GmbH, 2022.

610 Thompson, G., Scholzen, C., O'Donoghue, S., Haughton, M., Jones, R. L., Durant, A., and Farrington, C.: On the fidelity of high-resolution numerical weather forecasts of contrail-favorable conditions, Atmospheric Research, 311, 107 663, https://doi.org/10.1016/j.atmosres.2024.107663, 2024.

Tompkins, A. M., Gierens, K., and Rädel, G.: Ice supersaturation in the ECMWF integrated forecast system, Quarterly Journal of the Royal Meteorological Society, 133, 53–63, https://doi.org/10.1002/qj.14, 2007.

615   University of Utah: GOES-16/17/18 on Amazon Download Page, https://home.chpc.utah.edu/~u0553130/Brian_Blaylock/cgi-bin/goes16_
       download.cgi, 2020.

       University of Wyoming: Atmospheric Soundings, https://weather.uwyo.edu/upperair/sounding.html, 2024.

       Unterstrasser, S.: Large-eddy simulation study of contrail microphysics and geometry during the vortex phase and consequences on contrail-
       to-cirrus transition, Journal of Geophysical Research: Atmospheres, 119, 7537–7555, https://doi.org/10.1002/2013JD021418, 2014.

620   Unterstrasser, S.: Properties of young contrails; a parametrisation based on large-eddy simulations, Atmospheric Chemistry and Physics, 16,
       2059–2082, https://doi.org/10.5194/acp-16-2059-2016, 2016.

       Zhang, C. and Harrington, J. Y.: Including Surface Kinetic Effects in Simple Models of Ice Vapor Diffusion, Journal of Atmospheric Sciences,
       71, 372–390, https://doi.org/10.1175/JAS-D-13-0103.1, 2014.